Supporting Information for:

Kinetic and Mechanistic Assessment of Alkanol/Alkanal Decarbonylation and Deoxygenation Pathways on Metal Catalysts

Elif I. Gürbüz[1,2], David D. Hibbitts[1], and Enrique Iglesia[1,2*]

[1]Department of Chemical and Biomolecular Engineering, University of California at Berkeley

[2]Division of Chemical Sciences, E.O. Lawrence Berkeley National Laboratory, Berkeley, CA, 94720

*to whom correspondence should be addressed: iglesia@berkeley.edu

Table of Contents

List of Figures

S1. Details of Experimental Procedures

S1.1. Treatment Conditions for Synthesized Catalysts

All samples were heated to 393 K at 1 K min^{-1} in flowing dry air (Praxair, 99.99%, 5.0 cm^3 g^{-1} s-^{1}) and held for 8 h at 393 K. Ir (1.0% wt.), Ru and Cu catalysts were subsequently heated at 2 K min^{-1} to 548 K and held for 1 h in flowing dry air. Samples were cooled to ambient temperature and then heated at 2 K min^{-1} to 673 K in flowing 50% H_2/He (Praxair, 99.999%, 1.0 cm^3 g^{-1} s^{-1}) and held for 3 h. Ir (2.0% wt.) was heated at 2 K min^{-1} to 673 K and held for 2 h in flowing dry air, cooled to ambient temperature and then heated to 723 K at 2 K min^{-1} in flowing 50% H_2/He (Praxair, 99.999%, 1.0 cm^3 g^{-1} s^{-1}) and held for 3 h. Ir (3.0% wt.) was heated at 2 K min^{-1} to 1123 K and held for 12 h in flowing dry air, cooled to ambient temperature and then heated at 2 K min^{-1} to 1173 K in flowing 50% H_2/He (Praxair, 99.999%, 1.0 cm^3 g^{-1} s^{-1}) and held for 8 h. Pt/SiO_2 was heated to 723 K at 1 K min^{-1} in flowing 50% H_2/He and held for 3 h. All samples were cooled to ambient temperature and passivated in flowing 0.5% O_2/He (Praxair, 99.99%, 1.0 cm^3 g^{-1} s^{-1}) for 3 h before exposure to ambient air.

S1.2. TEM Measurements and Dispersion Calculations

For Cu, the cluster size distribution was determined by TEM imaging (Philips/FEI Tecnai 12 microscope at 120 kV) using samples suspended in ethanol and dispersed onto ultrathin carbon/holey carbon films supported on 400 mesh Cu grids (Ted Pella Inc.). Size distributions of metal clusters were determined from measuring more than 300 clusters. Surface-averaged cluster diameter was calculated to be 5.1 nm using:

$$< \mathrm{d_{TEM}} > = \frac{\sum \mathrm{n_i d_i}^3}{\sum \mathrm{n_i d_i}^2} \tag{S1}$$

S1.3. Temperature, Pressure, Gas and Liquid Flow Controls in the Flow Reactor

The reactor was thermostated within a three-zone resistively-heated furnace and the bed temperature was measured using a type K thermocouple held within a 1/16” stainless steel sheath. Pressure was controlled using a dome-loaded regulator (Mity-Mite, S91XW). Reactant concentrations were set using electronic mass flow controllers (Parker, Model 201) for H_2 (Praxair, 99.999%) and CO (Praxair, 1% in He) streams and a liquid syringe pump (ISCO 65DM; for 1-butanol and H_2O). Liquids were vaporized into H_2 flow at 443 K and all species maintained in their gaseous state by heating all transfer lines to 443 K.

S2. Details of Computational Methods

Gas-phase species were calculated within using 18 x 18 x 18 Å unit cells. Surfaces were modeled as a 4x4 Ir(111) closed-packed surface with an fcc lattice parameter of 3.84 Å;[1] with four layers perpendicular to the (111) surface. The bottom two layers were kept at their bulk positions and the topmost two layers were relaxed to their minimum energy positions. Additional calculations were run with similar protocols to determine the CO* and C* binding energies on other transition metals (Cu(111), Rh(111), Pd(111), Ru(0001), and Pt(111)).

Energies were converged to within 10^{-6} eV. Forces were computed using a fast Fourier transform (FFT) grid with a cutoff of twice the planewave cutoff, and a 3 x 3 x 1 Monkhorst-pack sampling of the first Brillouin zone (k-point mesh).[41] Structural optimization continued until the force on unconstrained atoms was <0.05 eV/Å. After geometric convergence, a single-point calculation with a 6 x 6 x 1 k-point mesh was performed to refine the energies of reactants, products, and transition states for each elementary step. Transition state (TS) structures were obtained for each elementary reaction using the nudged elastic band (NEB) method[2] and the dimer method.[3] NEB calculations were carried out using 16 images to provide an estimate of the reaction path and a starting point for the transition state structure and the vibrational mode along the reactive coordinate. The dimer algorithm was then used to locate the transition state using the optimization protocols described above.

Frequency calculations were performed on all optimized states (including transition states) to determine zero-point vibrational energies ($ZPVE$), vibrational enthalpies (H_{vib}), and free energies (G_{vib}). These terms were then used, together with electronic energies (E_0, provided by VASP), to estimate enthalpies:

---

[1] Singh, H. *Acta Cryst.* **1968**, *24*, 469.

[2] Henkelman, G.; Jonsson, H. A. *Journal of Chemical Physics* **2000**, *113*, 9978. Jonsson, H. A.; Mills, G.; Jacobsen, K. W. *Nudged Elastic Band Method for Finding Minimum Energy Paths of Transitions*; World Scientific, 1998.

[3] Henkelman, G.; Jonsson, H. A. *Journal of Chemical Physics* **1999**, *111*, 7010.

$$H = E_0 + ZPVE + H_{vib} + H_{trans} + H_{rot} \tag{S2}$$

and free energies:

$$G = E_0 + ZPVE + G_{vib} + G_{trans} + G_{rot} \tag{S3}$$

for all reactants, products, and transition states. In Equations S2 and S3, *ZPVE* is the zero-point vibrational energy, H_{vib}, H_{trans}, and H_{rot} are vibrational, translational, and rotational enthalpies (with similar symbols for free energies in Eq. S3: G_{vib}, G_{trans}, and G_{rot}). All transition states were confirmed to have a single negative frequency, corresponding to the vibrational mode along the reaction coordinate. H_{trans}, H_{rot}, G_{trans}, and G_{rot} were computed from statistical mechanics for the gaseous forms of all molecules involved. The enthalpy of a given state can be written as the sum of the DFT-derived energy (E_0), zero-point vibrational enthalpy (*ZPVE*) and vibrational, translational and rotational enthalpy (H_{vib}, H_{trans} and H_{rot}):

$$H = E_0 + ZPVE + H_{vib} + H_{trans} + H_{rot} \tag{S4}$$

similarly, the free energy of a state can be written as:

$$G = E_0 + ZPVE + G_{vib} + G_{trans} + G_{rot} \tag{S5}$$

and entropy can be determined for a state with a known *H* and *G* at a given *T*:

$$S = \frac{H - G}{T} \tag{S6}$$

For calculations which include a periodic Ir(111) surface (including adsorbed species and transition states on that surface), there are no translational or rotational degrees of freedom and DFT-derived vibrational frequencies can be used to determine the *ZPVE*, H_{vib} and G_{vib} shown in Eqns. S7-9.

$$ZPVE = \sum_i (½ \nu_i h) \tag{S7}$$

$$H_{vib} = \sum_i \left(\frac{\nu_i h e^{\frac{-\nu_i h}{kT}}}{1 - e^{\frac{-\nu_i h}{kT}}} \right) \tag{S8}$$

$$G_{vib} = \sum_i \left(-kT \ln \frac{1}{1 - e^{\frac{-\nu_i h}{kT}}} \right) \tag{S9}$$

Gas-phase molecules have translational and rotational degrees of freedom; thus H_{trans}, H_{rot}, G_{trans} and G_{rot} must also be computed:[4]

$$H_{trans} = {}^{5}\!/_{2}\, kT \tag{S10}$$

$$H_{rot,linear} = kT \tag{S11}$$

$$H_{rot,nonlinear} = {}^{3}\!/_{2}\, kT \tag{S12}$$

$$G_{trans} = -kT \ln\left[\left(\frac{2\pi MkT}{h^2}\right)^{3/2} V\right] \tag{S13}$$

$$G_{rot} = -kT \ln\left[\frac{\pi^{1/2}}{\sigma}\left(\frac{T^3}{\theta_x\theta_y\theta_z}\right)^{1/2}\right] \tag{S14}$$

$$\theta_i = \frac{h^2}{8\pi^2 I_i k} \tag{S15}$$

where I_i is the moment of inertia about axes x, y or z and σ is the symmetry number of the molecule.

Intrinsic enthalpy and free energy barriers (ΔH_{act} or ΔG_{act}, respectively) denote here the differences in enthalpy or free energy between a transition state and its precursor reactants for each elementary step. Effective activation enthalpies ($\Delta H^{\ddagger}$) and free energies ($\Delta G^{\ddagger}$) denote the change in enthalpy or free energy in forming the transition state from the alkanol reactant in its gaseous state; the latter are used here to compare different sequences of elementary steps with respect to the same reference state.

Co-adsorbed CO* was not included in the calculations, even though rate data were obtained at conditions leading to surfaces partially covered with CO* (Section 3.1 and 3.2), to decrease the configurational diversity associated with modeling reactions at intermediate coverages. We surmise that CO* coverages influence the values of the effective enthalpy and free energy barriers, but that differences in such barriers among the various plausible routes considered will depend on CO* coverage only weakly, as shown for the calculated effects of NO* coverage on NO-H_2 reactions.[5]

---

[4] McQuarrie, D, *Statistical Mechanics*, 2000, University Science Books, Sausolito, CA.

[5] Hibbitts, D.; Jiménez, R.; Yoshimura, M.; Weiss, B.; Iglesia, E. *J. Catal.* **2014**, *319*, 95.

S3. Catalyst Stability

Decarbonylation and C-O hydrogenolysis turnover rates were stable with time on stream (Fig. S1), indicating that CO* did not irreversibly poison the Ir metal, but instead inhibited rates through quasi-equilibrated adsorption/desorption events.

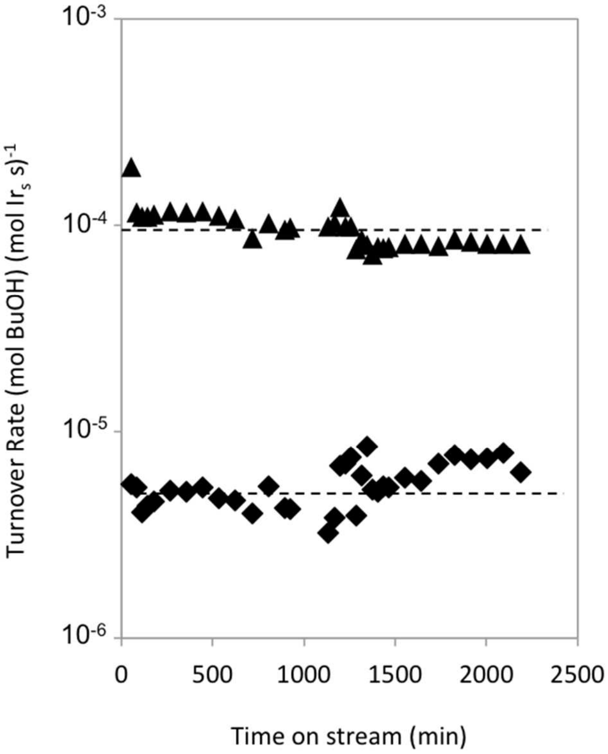

Figure S1. Decarbonylation (▲) and C–O hydrogenolysis (♦) turnover rates on Ir/SiO_2 (0.7 nm) with time on stream (483 K, 5 kPa 1-butanol, 1 kPa CO, 2 MPa H_2). Dashed lines represent trends.

S4. Coverage of H* during Alkanol/Alkanal Decarbonylation at High H_2 Pressures

Larger Ir clusters expose a larger fraction of surface atoms at low-index terraces, where adsorbed species (H*, CO*, and 1-butanol-derived intermediates) would bind more weakly than at corner and edge low-coordination atoms, which prevail on smaller clusters. Yet, H_2 pressure effects for decarbonylation rates are similar on Ir clusters with different mean diameters (Fig. S2a, 0.7-7 nm). These similar kinetic effects may reflect: i) H* coverages that depend on H* binding energies, but which are influenced by size to the same extent as CO* and 1-butanol derived intermediates) on saturated surfaces or ii) H* coverages that are not kinetically-detectable at these conditions (1-5 kPa 1-butanol, 1-3 MPa H_2, 0.8-8 kPa CO at 523 K). The insensitivity of C–O hydrogenolysis rates to H_2 pressure (Fig. 2b and S2b) is, however, more consistent with (ii), because any significant H* coverage on Ir sites would likely inhibit both C–O hydrogenolysis and decarbonylation. In contrast with alkanol/alkanal decarbonylation, Ir cluster surfaces are saturated with H* at similar H_2 pressures (0.6-2 MPa H_2) during alkane hydrogenolysis.[6] These low H* coverages during 1-butanol-butanal reactions (Ir (0.7 nm), 523 K, 0.8-3 MPa H_2, 0.8-10 kPa CO) appear to reflect H_2 dissociative adsorption enthalpies ($\Delta H_{ads,H2}$) that become less negative (and ultimately positive) as CO* coverages increase (0.30 to 0.85 ML at 0.8-10 kPa CO in this study); CO(g) and CO* are not present in alkane hydrogenolysis reactions. DFT-derived $\Delta H_{ads,H2}$ values range from –52 to +26 kJ mol^{-1} as CO* coverages increase from 0 to 0.75 ML CO* (Fig. S3), thus leading to very low H* coverages at the CO* coverages (> 0.30 ML) indicated by prevalent CO* inhibition at all conditions.

---

[6] Flaherty, D. W.; Hibbitts, D. D.; Gürbüz, E. I.; Iglesia, E. *J. Catal.* **2014**, *311*, 350. Flaherty, D. W.; Iglesia, E. *J. Am. Chem. Soc.* **2013**, *135*, 18586.

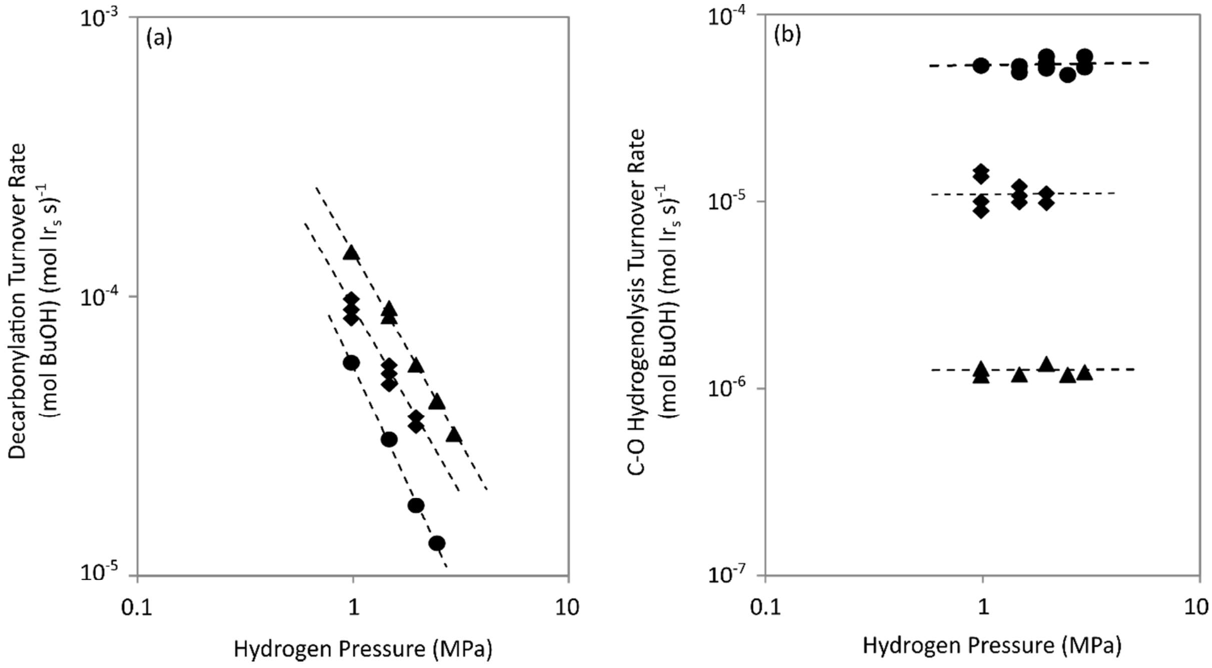

Figure S2. Effect of H_2 pressure on decarbonylation (a) and C–O hydrogenolysis (b) turnover rates on Ir/SiO_2 (0.7 nm) (▲), 3.6 nm (♦), and 7.0 nm (●) (483 K, 5 kPa 1-butanol, 1 kPa CO, 0.5 kPa CO for 0.7 nm Ir clusters). Dashed lines represent trends.

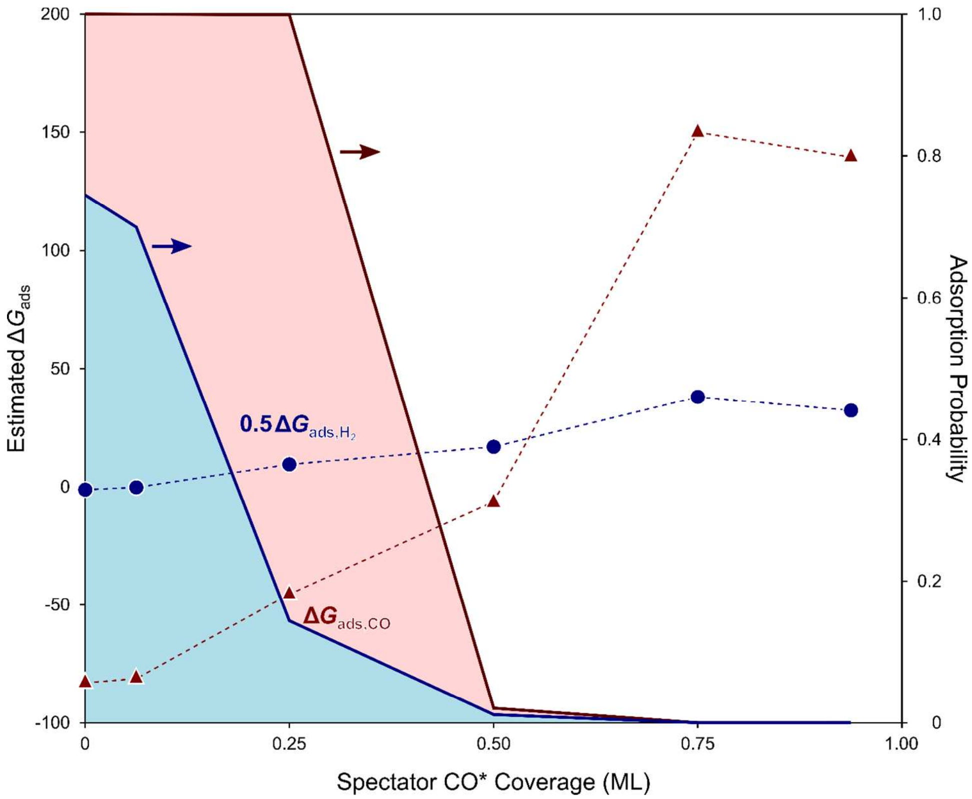

Figure S3. DFT-calculated adsorption free energies (left-axis) and probabilities (right-axis) for H* (from H_2) and CO* on surfaces with 0-15/16 ML of spectator CO* coverage.

Adsorption free energies for both H* (from H_2, $0.5\Delta G_{\text{ads,H2}}$) and CO* increase with increasing CO* coverage (Fig. S3), due to repulsive through-space and through-surface interactions between co-adsorbates. CO*–CO* repulsions are stronger than CO*–H* repulsions, as ΔG_{ads} for CO* increases from −85 to +158 kJ mol^{-1} and those for H* increase from +2 to +40 kJ mol^{-1} as (spectator) CO* coverage increases from 0 to 15/16 ML. Dissociative H_2 adsorption, however, is much less exothermic (and exergonic) than CO* adsorption at low coverages, which result in moderate (near 0.5 ML) CO* coverages suppressing H* adsorption at lower CO* coverages than those which would suppress CO* adsorption, as shown by adsorption probabilities (shaded areas, calculated at 2MPa H_2 and 1 kPa CO) in Fig. S3. Adsorption probabilities for H* decrease from ~0.7 to 0.14 as spectator CO* coverage increases from 0.06 to 0.25 ML despite the adsorption probabilities for CO* remaining near 1 over that same range in CO* coverage. This creates a surface of moderate CO* coverage with very little H* coverage. These adsorption free energies are estimated through vibrational frequency analyses to determine entropies of surface-bound H* and CO* species, which are known to underestimate entropies of adsorbed species. This indicates that these adsorption probabilities are underestimated, consistent with H*-covered surfaces observed at high temperatures (593 K) and similar H_2 pressures (2 MPa) in the absence of any CO*-source.[7] The difference between the two curves, however, is unlikely to be affected by errors in entropy estimates of H* and CO*, leading to a consistent picture of moderate CO* (but not H*) coverage at H_2 pressures which would (in the absence of CO) lead to H*-covered surfaces.

---

[7] D. Flaherty, D. Hibbitts, E. Iglesia, *J. Am. Chem. Soc.* 136 (2014) 9664; D. Flaherty, D. Hibbitts, E. Gurbuz, E. Iglesia, *J. Catal.* 311 (2014) 350. D. Flaherty, E. Iglesia, *J. Am. Chem. Soc.* 135 (2013) 18586.

S5. DFT-Calculated Reactant, Transition, and Product States for Alcohol Dehydrogenation, Decarbonylation, and C–O Hydrogenolysis

Figures S4-S15 show all DFT-calculated structures determined in this work on propanol decompositions on Ir(111) surfaces. These Figures are organized by reacting species as described below:

Figure S4	Reactions of Propanol ($CH_3CH_2CH_2OH$)		Pg.	13
	$CH_3CH_2CH_2OH + 2* \rightarrow CH_3CH_2CH_2* + OH*$	Rxn. 16		
	$CH_3CH_2CH_2OH + 2* \rightarrow CH_3CH_2CH*OH + H*$	Rxn. 18		
	$CH_3CH_2CH_2OH + 2* \rightarrow CH_3CH_2CH_2O* + H*$	Rxn. 17		
Figure S5	Reactions of Propoxide ($CH_3CH_2CH_2O*$)		Pg.	14
	$CH_3CH_2CH_2O* + * \rightarrow CH_3CH_2CH_2* + O*$	Rxn. 19		
	$CH_3CH_2CH_2O* + * \rightarrow CH_3CH_2CHO + * + H*$	Rxn. 20		
Figure S6	Reactions of Hydroxypropyl (CH_3CH_2CHOH*)		Pgs.	15-16
	$CH_3CH_2CH*OH + * \rightarrow CH_3CH_2CH* + OH*$	Rxn. 22		
	$CH_3CH_2CH*OH + * \rightarrow CH_3CH_2CHO + * + H*$	Rxn. 23		
	$CH_3CH_2CH*OH + * \rightarrow CH_3CH_2C*OH + H*$	Rxn. 24		
	$CH_3CH_2CH*OH + H* \rightarrow CH_3CH_2CH* + * + H_2O$	Rxn. 21		
Figure S7	Reactions of Hydroxypropylidene (CH_3CH_2COH*)		Pgs.	17-18
	$CH_3CH_2C*OH* \rightarrow CH_3CH_2C* + OH*$	Rxn. 26		
	$CH_3CH_2C*OH* + * \rightarrow CH_3CH_2C*O* + H*$	Rxn. 28 (SI)		
	$CH_3CH_2C*OH* + * \rightarrow CH_3CH*C*OH + H*$	Rxn. 29 (SI)		
	$CH_3CH_2C*OH* \rightarrow CH_3CH_2* + COH*$	Rxn. 27 (SI)		
Figure S8	Reactions of Propanal (CH_3CH_2CHO)		Pgs.	19-20
	$CH_3CH_2CHO + 2* \rightarrow CH_3CH_2CH* + O*$	Rxn. 25		
	$CH_3CH_2CHO + 3* \rightarrow CH_3CH_2C*O* + H*$	Rxn. 4		
	$CH_3CH_2CHO + 4* \rightarrow CH_3CH*CH*O* + H*$	Rxn. 3		
	$CH_3CH_2CHO + 3* \rightarrow CH_3CH_2C* + CH*O*$	Rxn. 2		
Figure S9	Reactions of Propanoyl (CH_3CH_2C*O*)		Pgs.	21
	$CH_3CH_2C*O* \rightarrow CH_3CH_2C* + O*$			
	$CH_3CH_2C*O* \rightarrow CH_3CH_2* + CO*$	Rxn. 6		
	$CH_3CH_2C*O* + * \rightarrow CH_3CH*C*O + H*$	Rxn. 9		

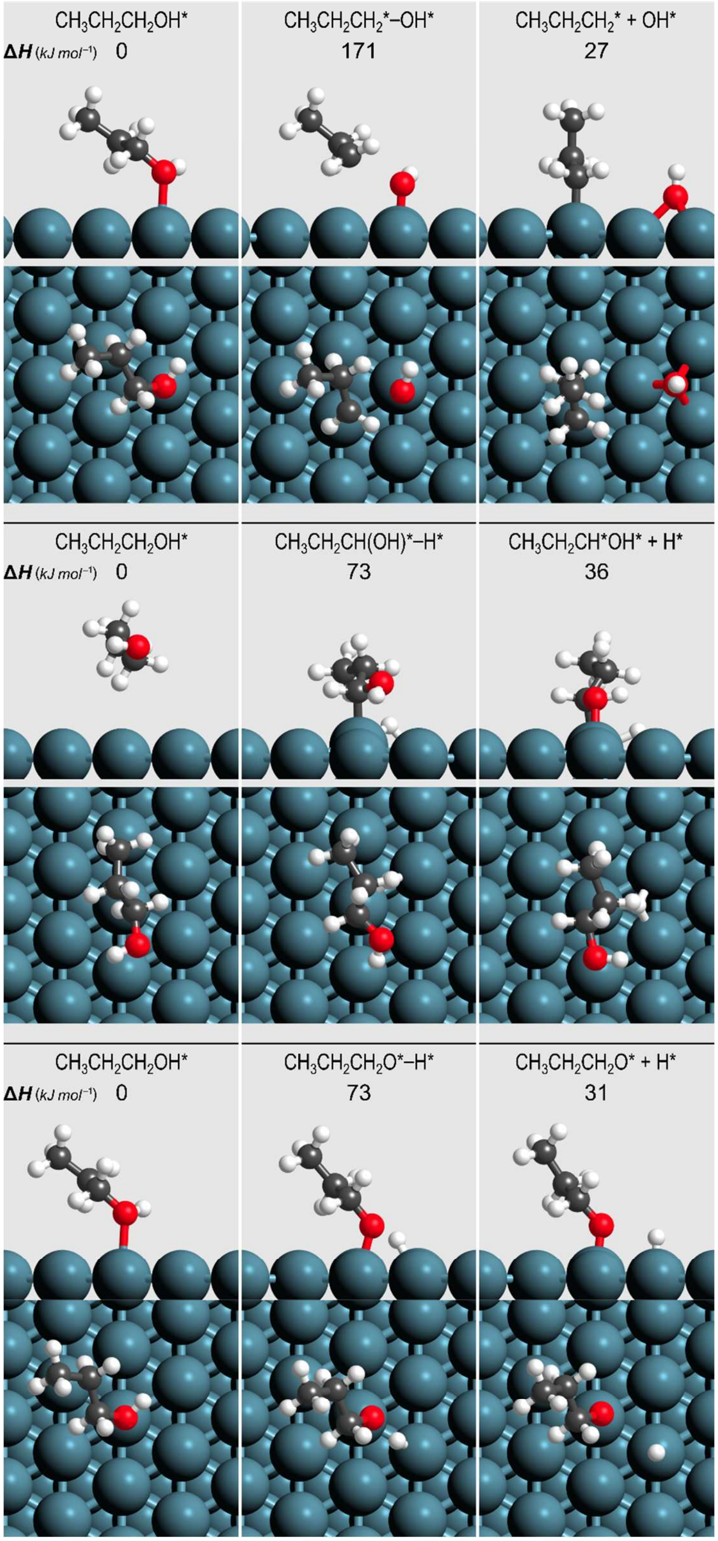

Figure S4. DFT-derived reactant, transition, and product states for reactions of 1-propanol ($CH_3CH_2CH_2OH$). Enthalpies of formation for each state (523 K) from a bare surface, gas-phase 1-propanol, and a stoichiometric amount of gas-phase H_2 are given in kJ mol^{-1}.

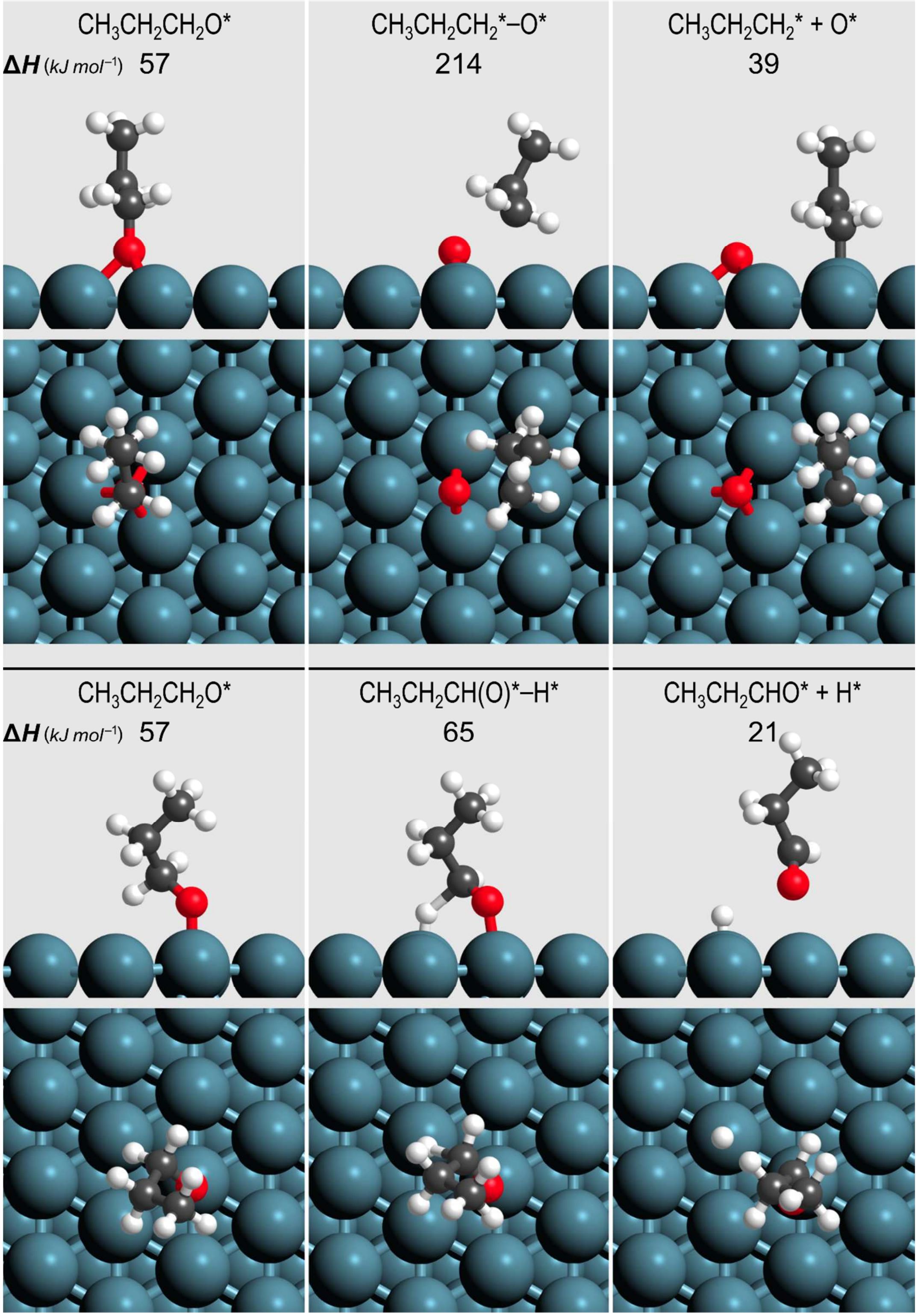

Figure S5. DFT-derived reactant, transition, and product states for reactions of propoxide ($CH_3CH_2CH_2O^*$). Enthalpies of formation for each state (523 K) from a bare surface, gas-phase 1-propanol, and a stoichiometric amount of gas-phase H_2 are given in kJ mol^{-1}.

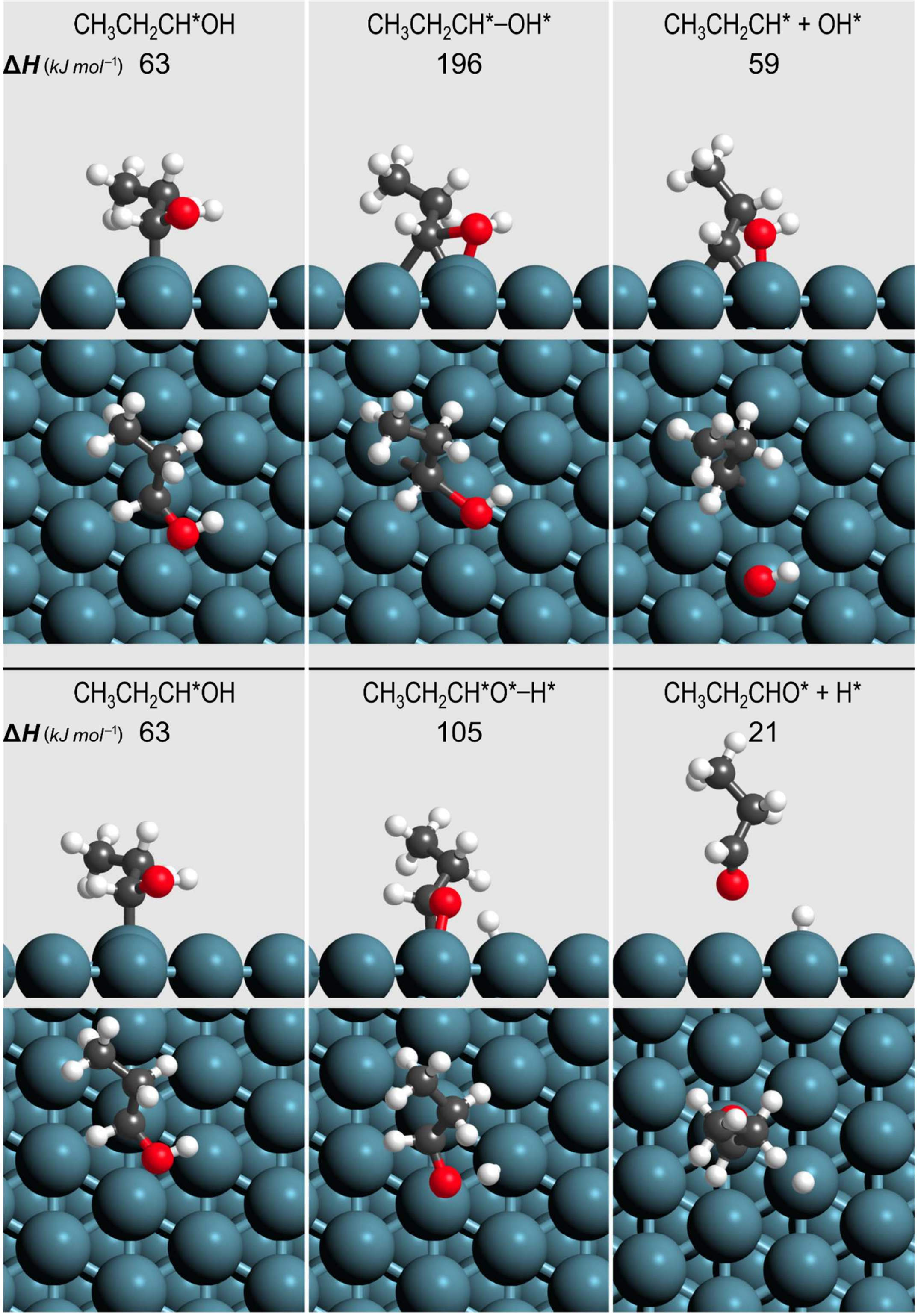

Figure S6. DFT-derived reactant, transition, and product states for reactions of hydroxypropyl ($CH_3CH_2CH^*OH$). Enthalpies of formation for each state (523 K) from a bare surface, gas-phase 1-propanol, and a stoichiometric amount of gas-phase H_2 are given in kJ mol^{-1}.

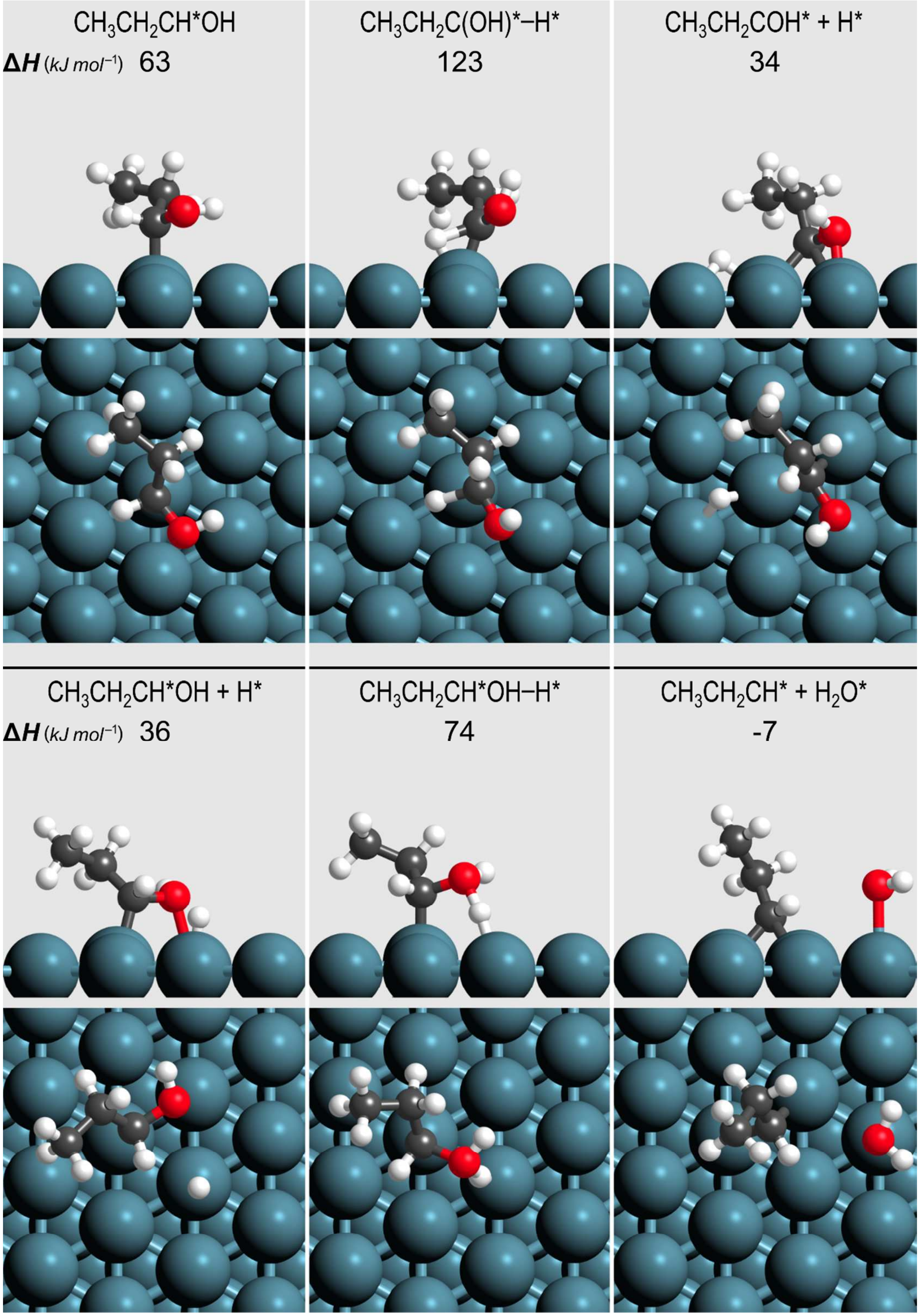

Figure S6. ***(Continued.)*** DFT-derived reactant, transition, and product states for reactions of hydroxypropyl ($CH_3CH_2CH^*OH$). Enthalpies of formation for each state (523 K) from a bare surface, gas-phase 1-propanol, and a stoichiometric amount of gas-phase H_2 are given in kJ mol^{-1}.

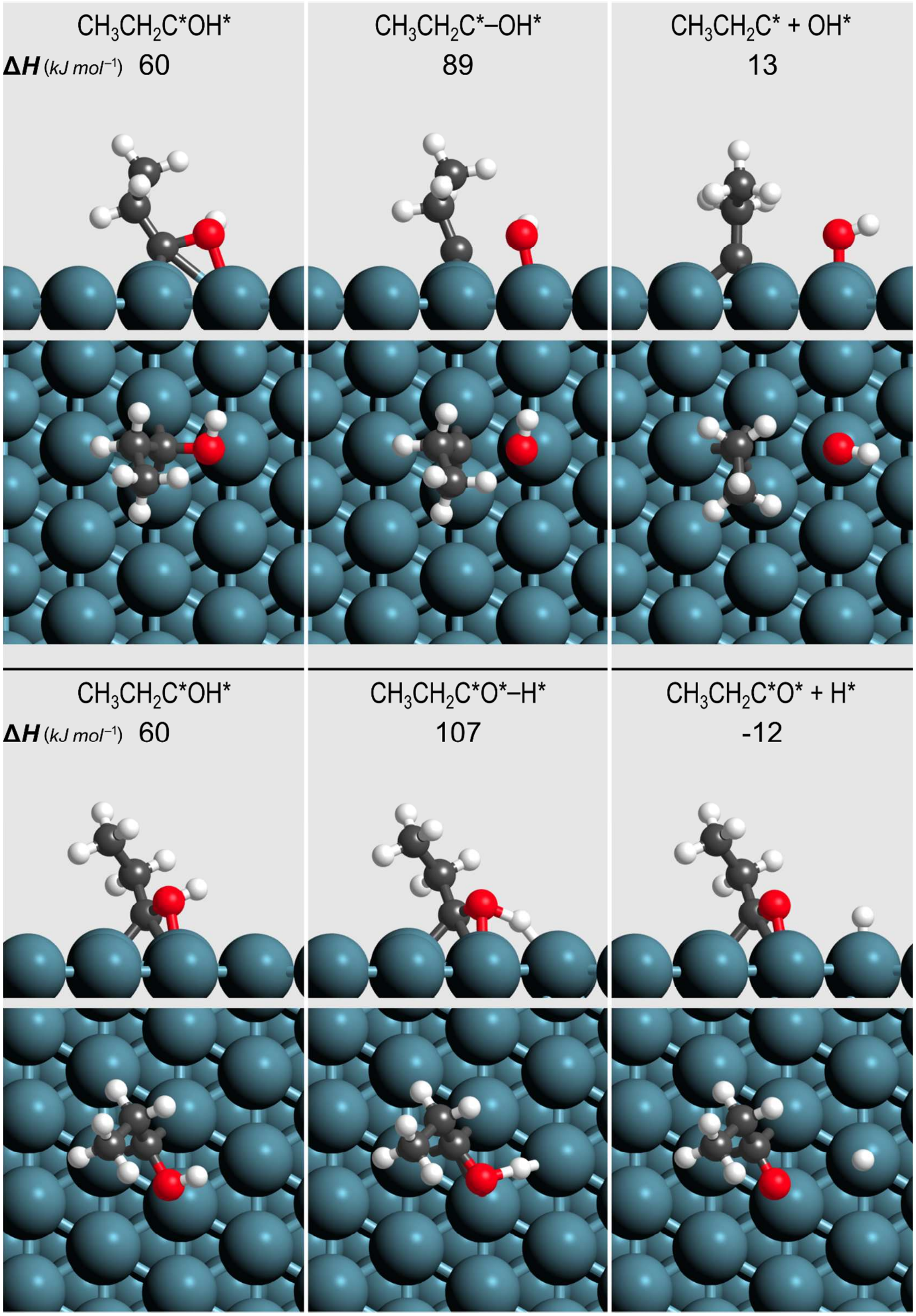

Figure S7. DFT-derived reactant, transition, and product states for reactions of hydroxypropylidene ($CH_3CH_2C^*OH$). Enthalpies of formation for each state (523 K) from a bare surface, gas-phase 1-propanol, and a stoichiometric amount of gas-phase H_2 are given in kJ mol^{-1}.

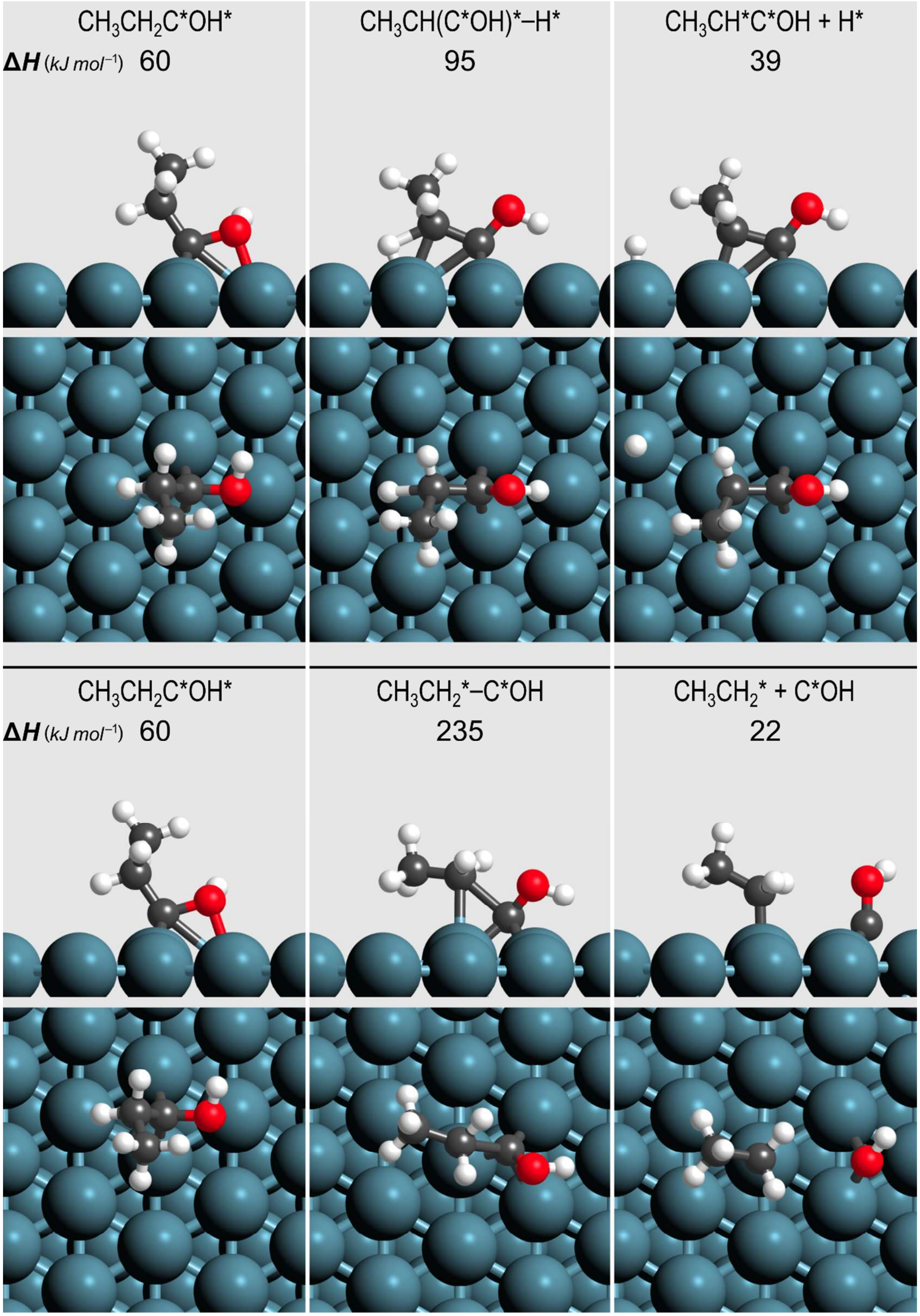

Figure S7. ***(Continued)*** DFT-derived reactant, transition, and product states for reactions of hydroxypropylidene (CH_3CH_2C*OH). Enthalpies of formation for each state (523 K) from a bare surface, gas-phase 1-propanol, and a stoichiometric amount of gas-phase H_2 are given in kJ mol^{-1}.

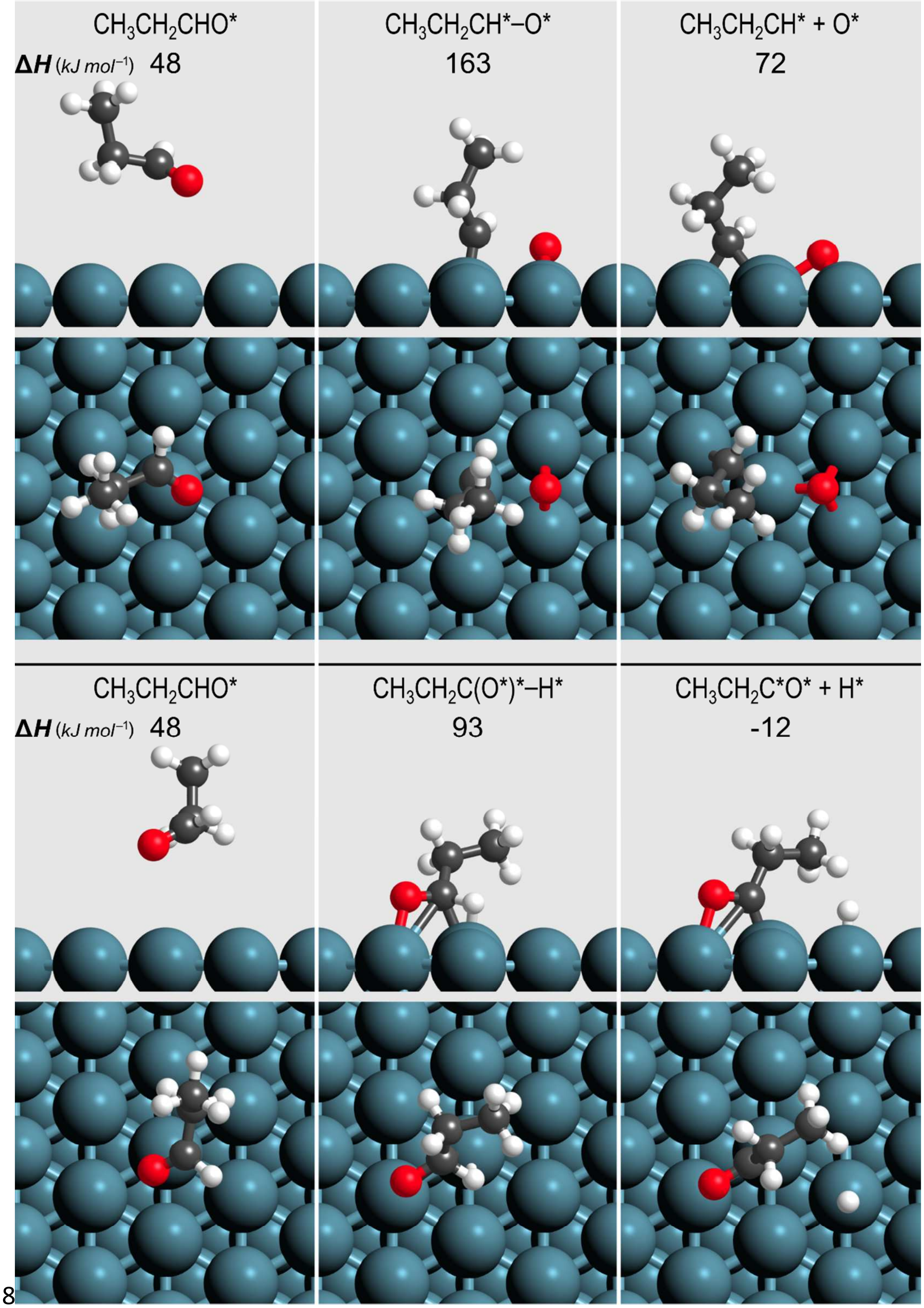

Figure S8. DFT-derived reactant, transition, and product states for reactions of propanal (CH_3CH_2CHO). Enthalpies of formation for each state (523 K) from a bare surface, gas-phase 1-propanol, and a stoichiometric amount of gas-phase H_2 are given in kJ mol^{-1}.

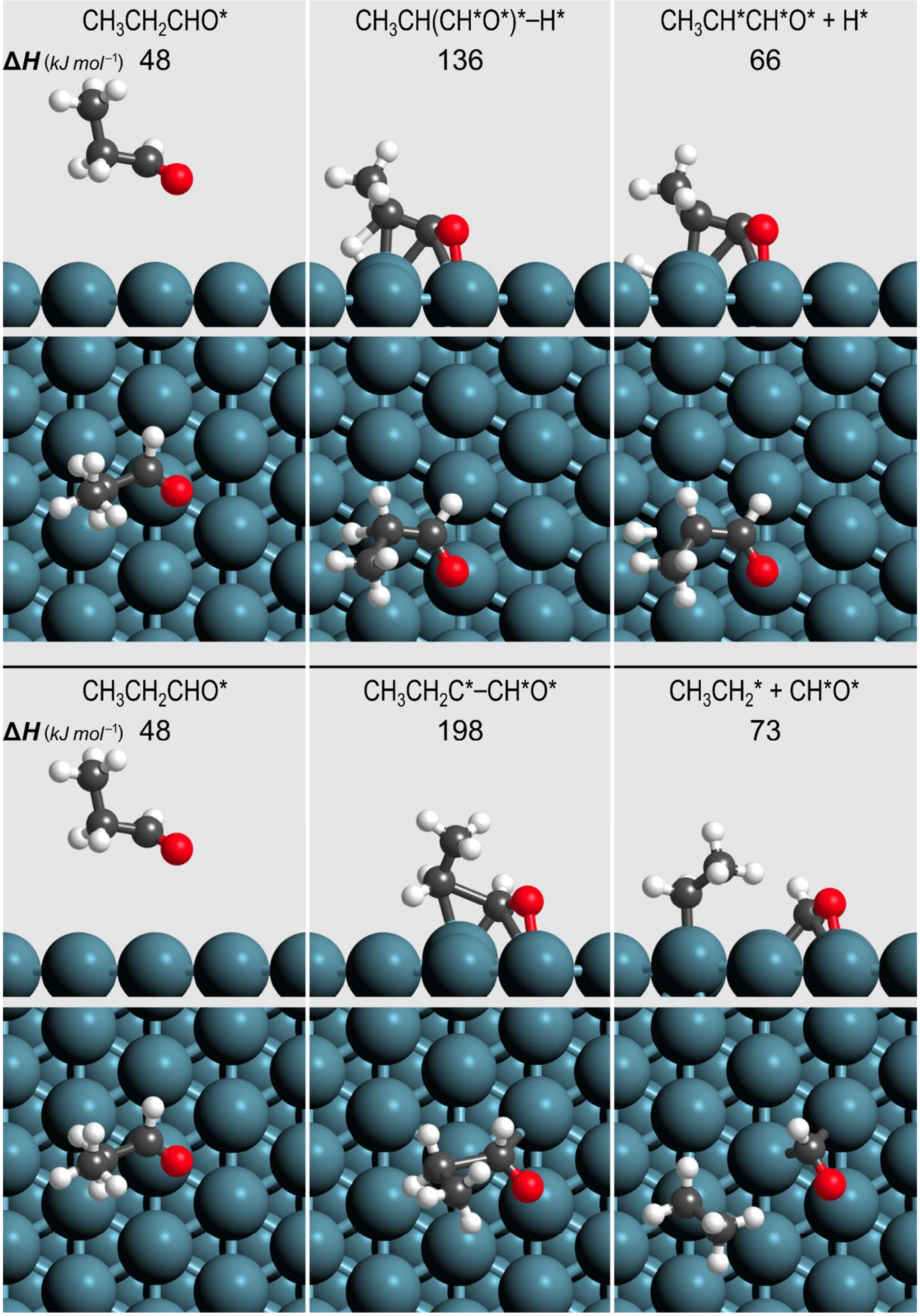

Figure S8. ***(Continued)*** DFT-derived reactant, transition, and product states for reactions of propanal (CH_3CH_2CHO). Enthalpies of formation for each state (523 K) from a bare surface, gas-phase 1-propanol, and a stoichiometric amount of gas-phase H_2 are given in kJ mol^{-1}.

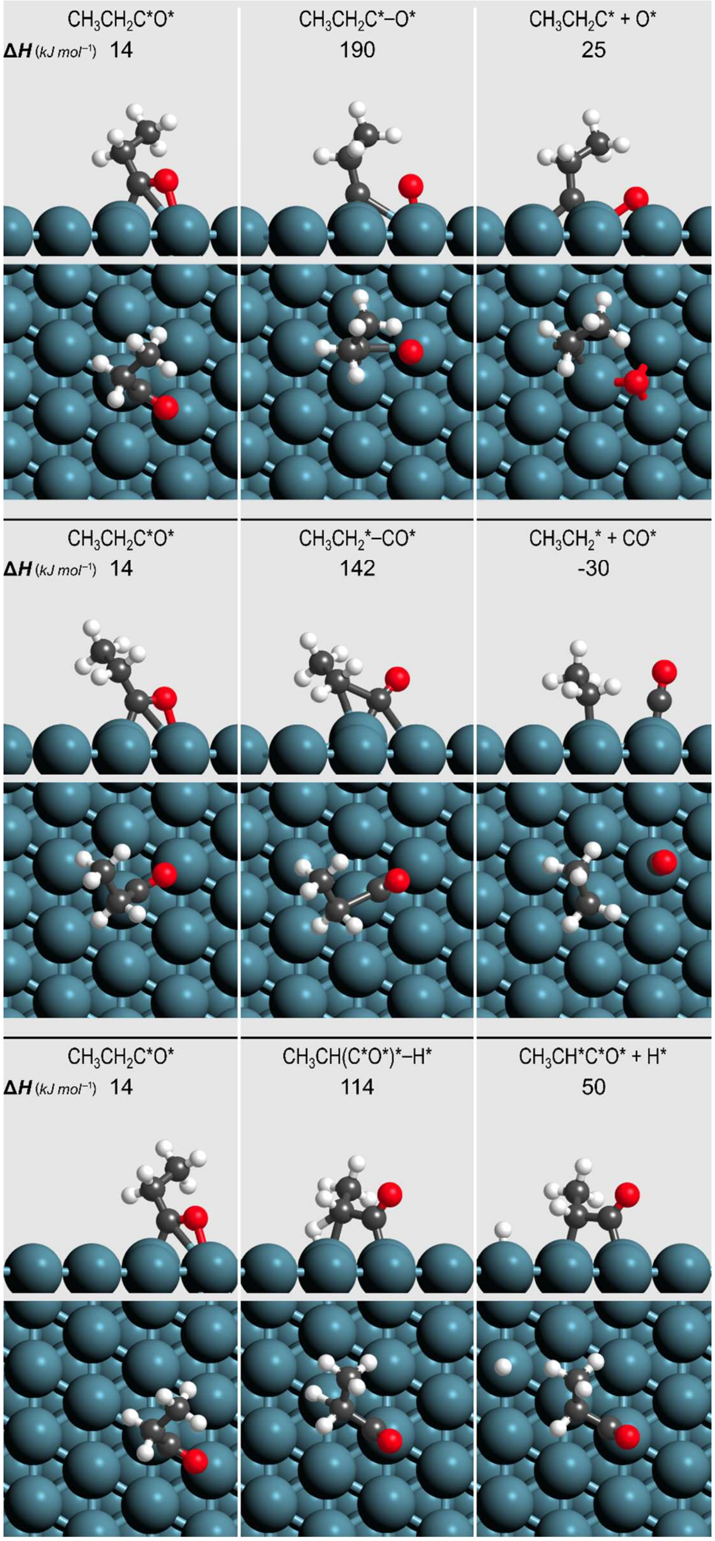

Figure S9. DFT-derived reactant, transition, and product states for reactions of propanoyl ($CH_3CH_2C^*O^*$). Enthalpies of formation for each state (523 K) from a bare surface, gas-phase 1-propanol, and a stoichiometric amount of gas-phase H_2 are given in kJ mol^{-1}.

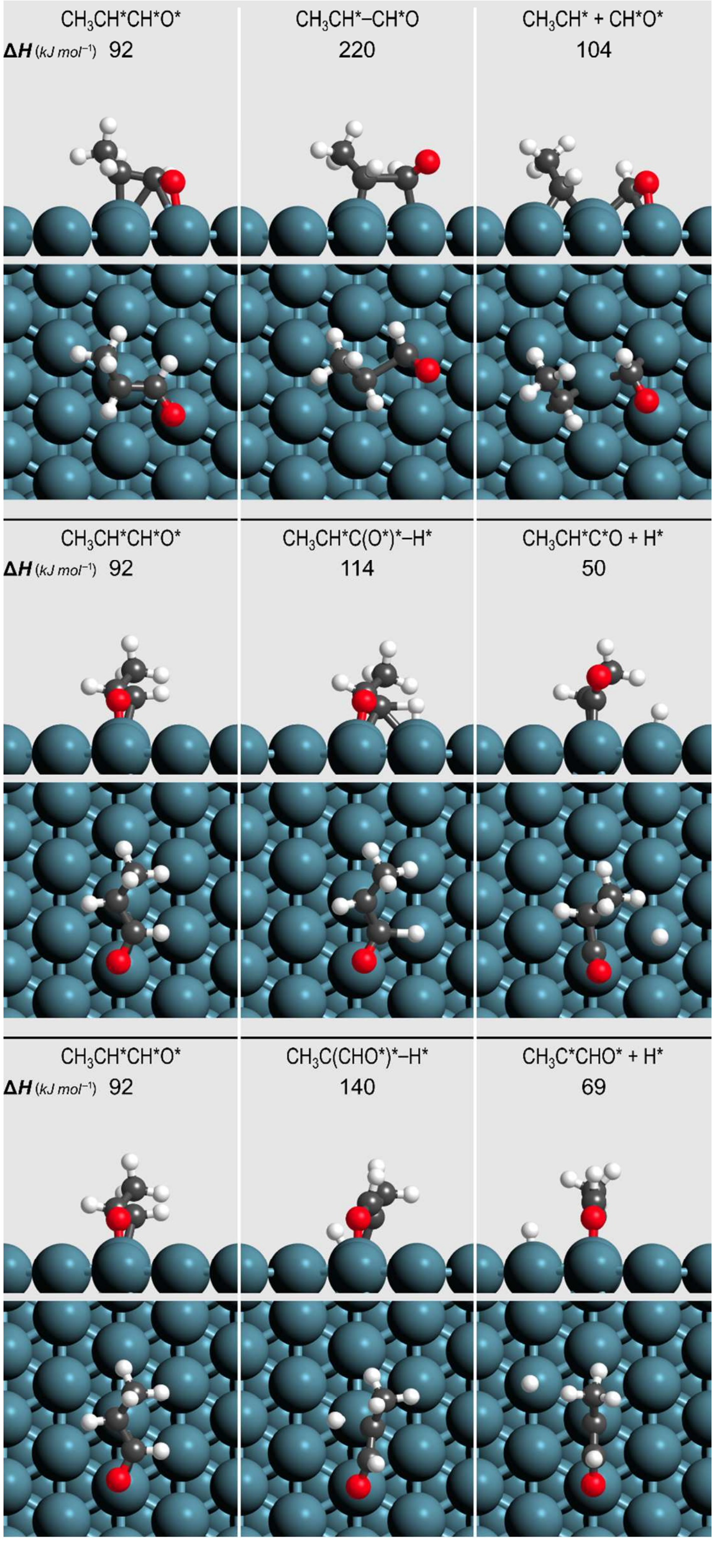

Figure S10. DFT-derived reactant, transition, and product states for reactions of $CH_3CH^*CH^*O^*$. Enthalpies of formation for each state (523 K) from a bare surface, gas-phase 1-propanol, and a stoichiometric amount of gas-phase H_2 are given in kJ mol^{-1}.

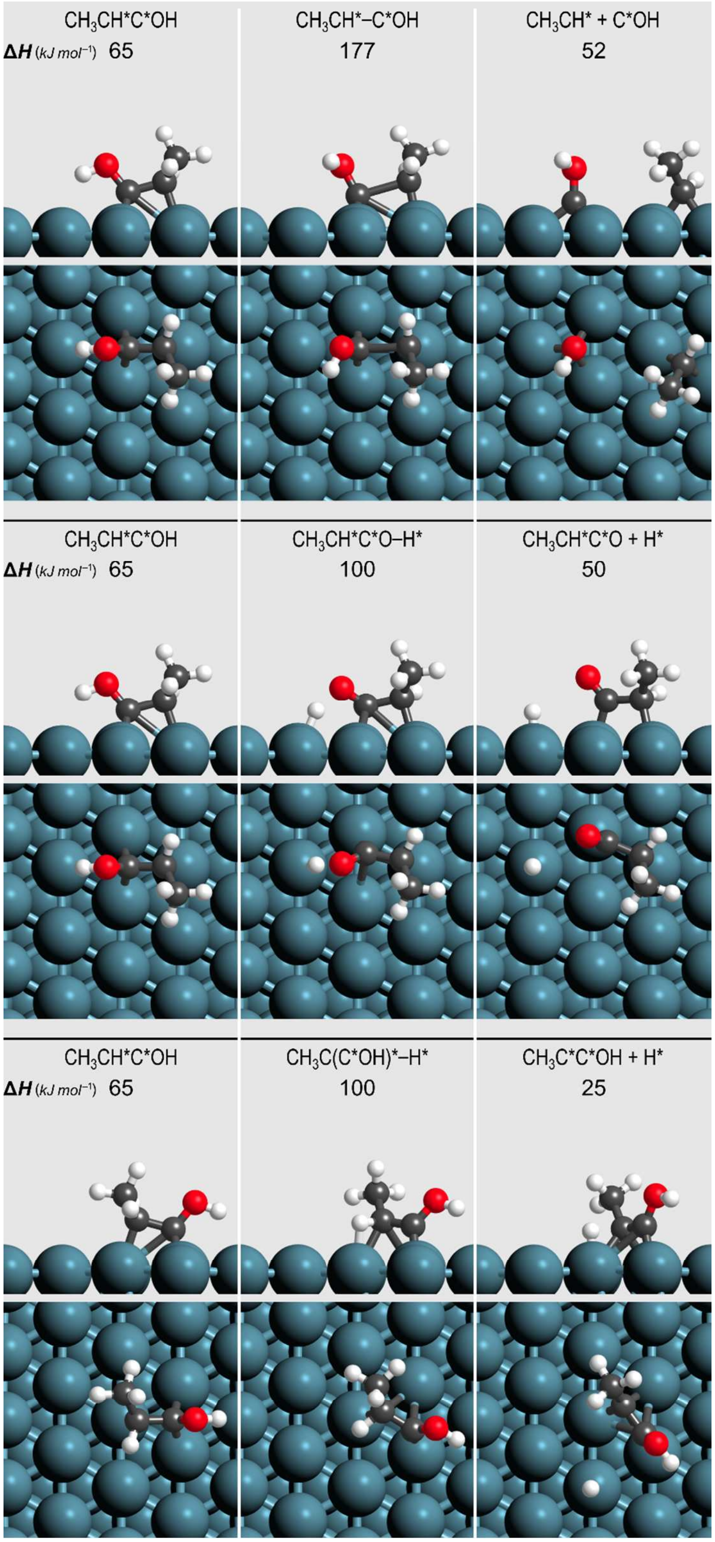

Figure S11. DFT-derived reactant, transition, and product states for reactions of $CH_3CH^*C^*OH$. Enthalpies of formation for each state (523 K) from a bare surface, gas-phase 1-propanol, and a stoichiometric amount of gas-phase H_2 are given in kJ mol^{-1}.

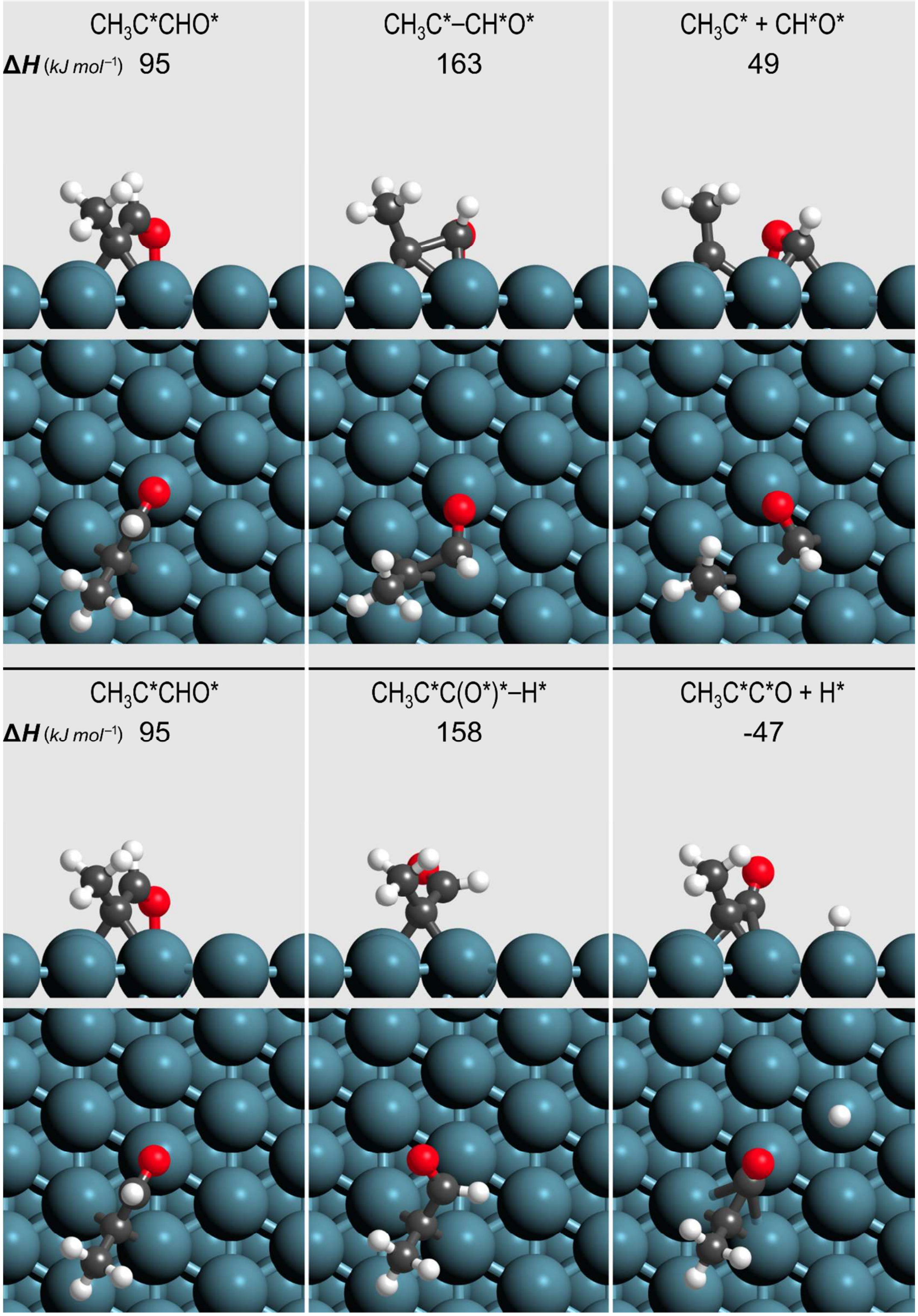

Figure S12. DFT-derived reactant, transition, and product states for reactions of $CH_3C^*CHO^*$. Enthalpies of formation for each state (523 K) from a bare surface, gas-phase 1-propanol, and a stoichiometric amount of gas-phase H_2 are given in kJ mol^{-1}.

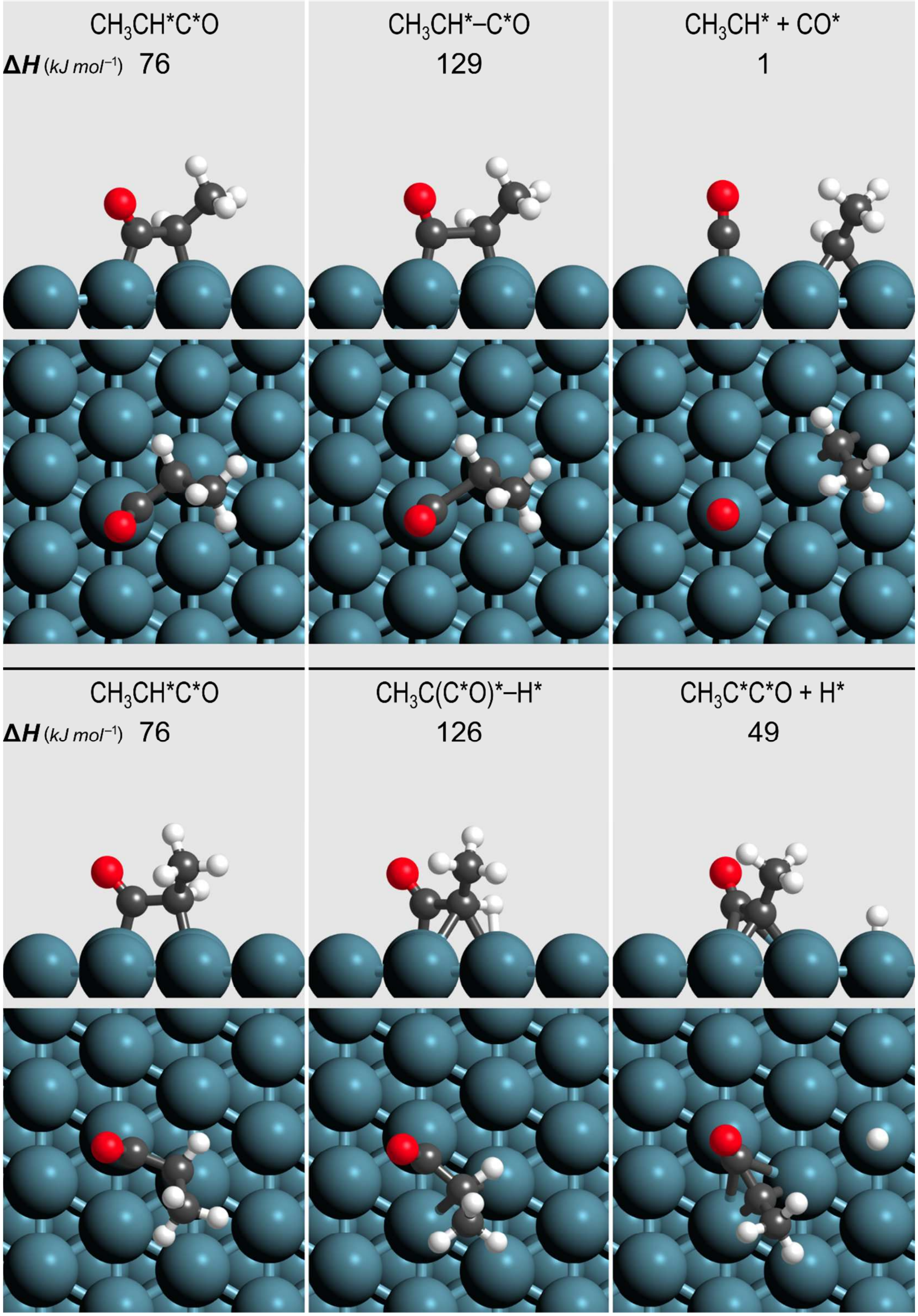

Figure S13. DFT-derived reactant, transition, and product states for reactions of $CH_3CH^*C^*O$. Enthalpies of formation for each state (523 K) from a bare surface, gas-phase 1-propanol, and a stoichiometric amount of gas-phase H_2 are given in kJ mol^{-1}.

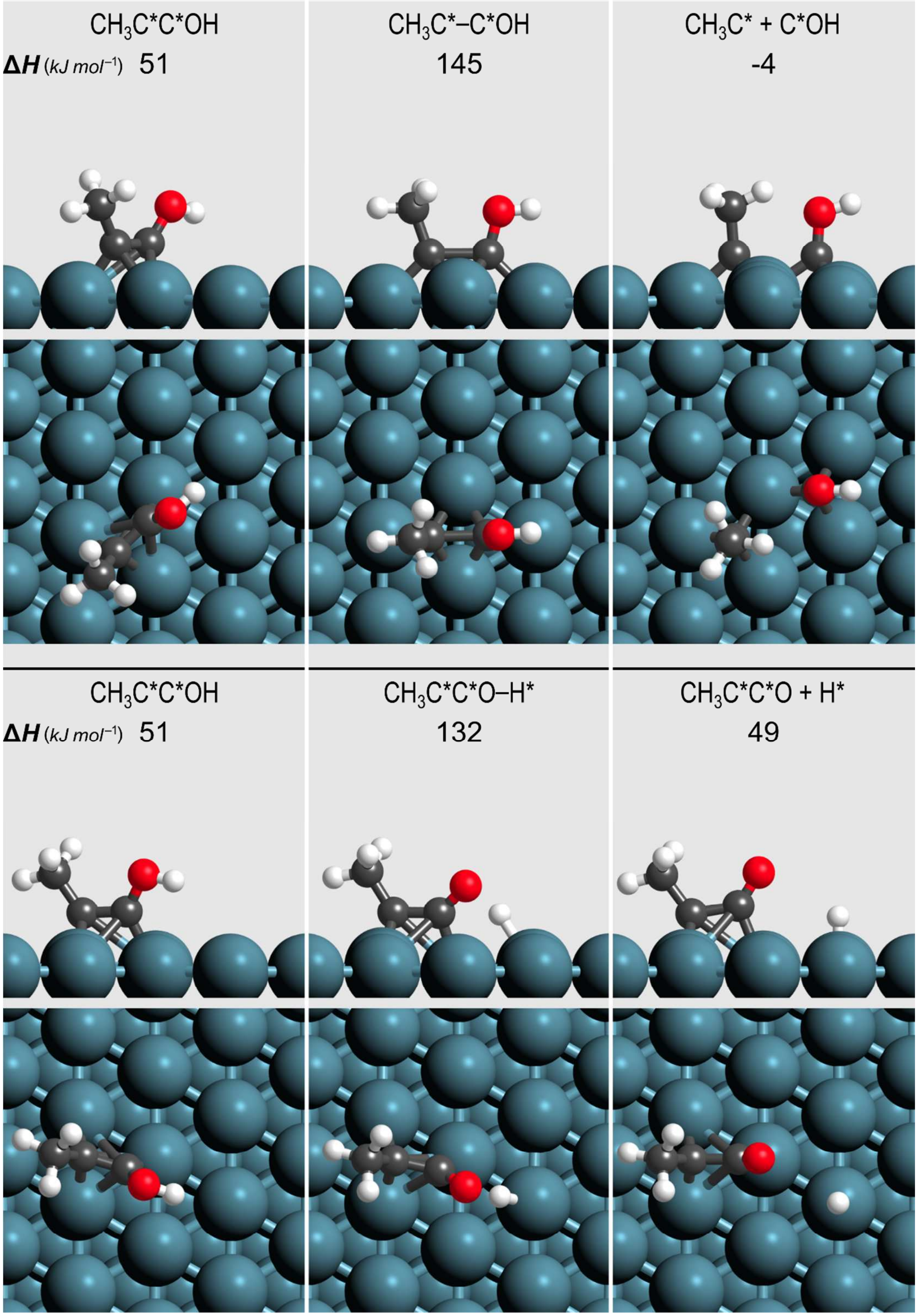

Figure S14. DFT-derived reactant, transition, and product states for reactions of $CH_3C^*C^*OH$. Enthalpies of formation for each state (523 K) from a bare surface, gas-phase 1-propanol, and a stoichiometric amount of gas-phase H_2 are given in kJ mol^{-1}.

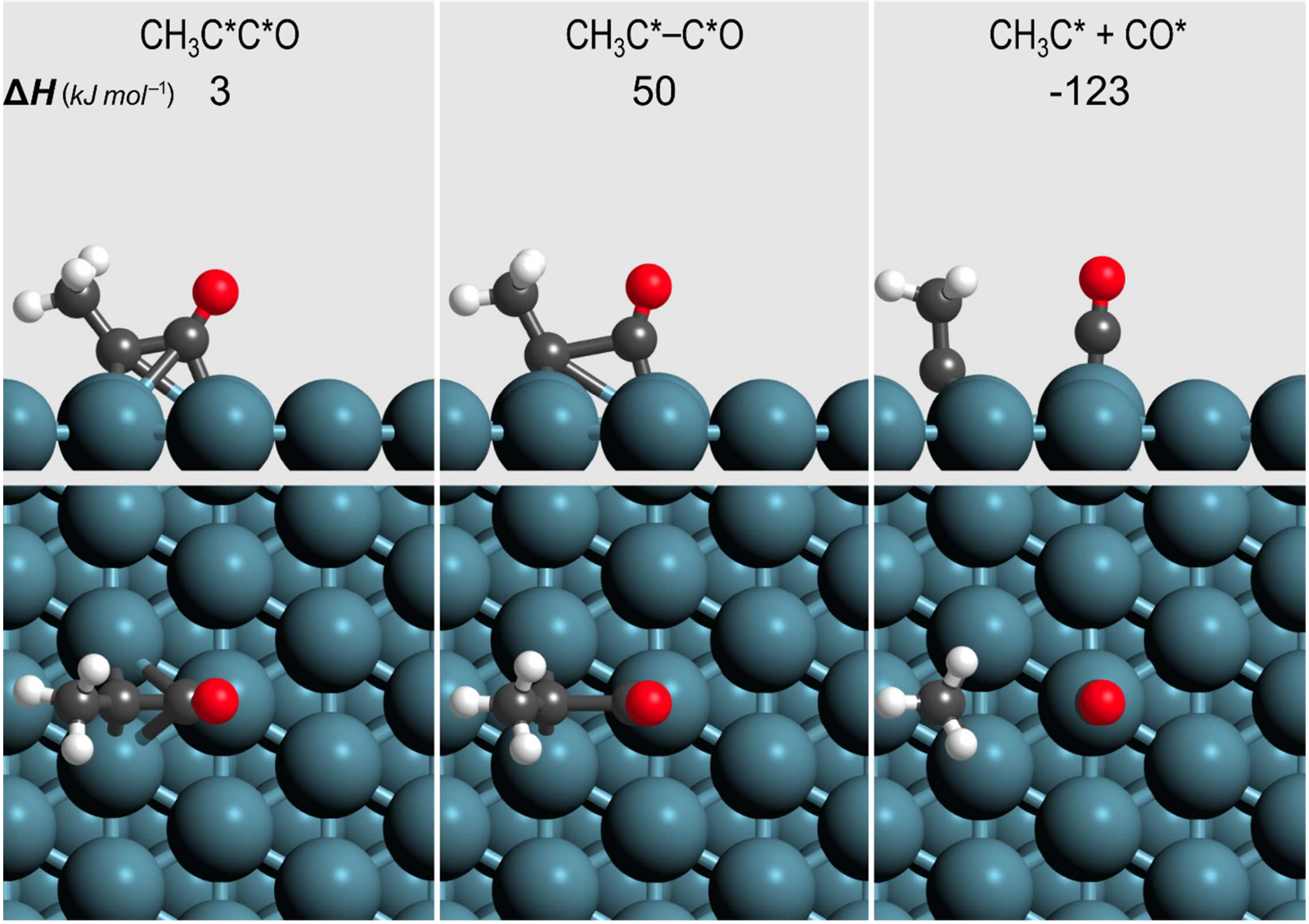

Figure S15. DFT-derived reactant, transition, and product states for reactions of $CH_3C^*C^*O$. Enthalpies of formation for each state (523 K) from a bare surface, gas-phase 1-propanol, and a stoichiometric amount of gas-phase H_2 are given in kJ mol^{-1}.

S6. Reaction Scheme for RC*OH species (R = CH_3CH_2, CH_3CH^*, CH_3C^*)

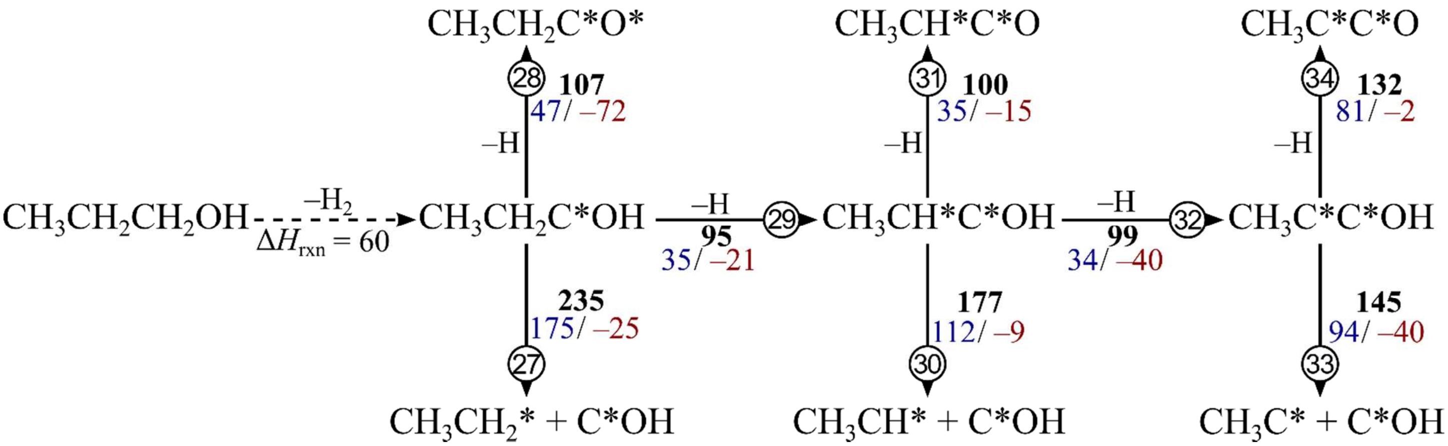

Scheme S1. DFT-calculated effective enthalpy barriers ($\Delta H^{\neq}$, black, bold typeface), intrinsic activation enthalpies (ΔH_{act}, blue, italic typeface), and reaction enthalpies (ΔH_{rxn}, red) for reactions of RC*OH species (R = CH_3CH_2, CH_3CH^*, CH_3C^*). Reaction numbers used throughout the text are given encircled (①, e.g.) on each reaction arrow.

S7. Discussion of Other C–O Activation Routes

Rate expressions for the routes mediated by these distinct steps can be derived using specific assumptions about the reversibility of each step. Next, we explore such assumptions by comparing for each species the rate of the step that reverses its formation with that for its consumption in later steps. The near-equilibrated nature of 1-butanol-butanal inter-conversions (Section 3.1) requires the concomitant near equilibration of all intervening adsorption (Step 15) and dehydrogenation (via $CH_3CH_2CH_2O^*$, Steps 17 and 20, or via $CH_3CH_2CH^*OH$, Steps 18 and 23) steps. C–O cleavage rates (and of decarbonylation) were not affected by H_2O, even when introduced at pressures (1 kPa) much higher than those present at 1-butanol reactions (< 0.003 kPa). These weak H_2O effects indicate that C–O bond cleavage steps (Steps 16, 19, 21, 22, 25, and 26) must be irreversible, because their net rates would otherwise be inhibited by the presence of H_2O-derived O* and OH* species that also form in C-O cleavage steps. DFT-derived free energies of formation of OH* or O* from gas-phase H_2O:

$$H_2O + * \leftrightarrow OH^* + \tfrac{1}{2} H_2 \tag{S16}$$

$$H_2O + * \leftrightarrow O^* + H_2 \tag{S17}$$

are 97 and 104 kJ mol^{-1}, respectively, consistent with small equilibrium constants (K_O and K_{OH}) and with low and kinetically-insignificant O* and OH*coverages at all relevant H_2O pressures.

C–H activation in $CH_3CH_2CH^*OH$ species forms $CH_3CH_2C^*OH$ (Step 24) with a much larger reverse barrier (89 kJ mol^{-1}) than for C–O activation in $CH_3CH_2C^*OH$ (29 kJ mol^{-1}). The ratio of the reverse rate of Step 24 to the forward rate of Step 26:

$$\frac{r_{-24}}{r_{26}} = \frac{[H^*]}{[*]} e^{-\left(\frac{\Delta H_{act,-24} - \Delta H_{act,26}}{RT}\right)} e^{\left(\frac{T\Delta S_{act,-24} - T\Delta S_{act,26}}{RT}\right)} \tag{S18}$$

determines the extent of equilibration for Step 24. The first exponential term is 4 x10^{-5} at 523 K and [H*]/[*] ratios are much less than unity (from the low prevalent H* coverages inferred from rate data and unfavorable H* adsorption energies on Ir(111) at elevated CO* coverages (Section 3.2, Fig. S3). The ΔS_{act} value for the reverse of Step 24 is likely to be smaller than that for Step 26, because the reverse of Step 24 is bimolecular

(H*-addition to $CH_3CH_2C^*OH$), while Step 26 (C–O activation of $CH_3CH_2C^*OH$) is unimolecular; as a result, the second exponential term is also much smaller than unity, making the rate ratio in Equation S18 also much smaller than unity. Thus, $CH_3CH_2C^*OH$ formation step is irreversible and the sole kinetically-relevant step if C–O hydrogenolysis reactions occurred via C–O cleavage in $CH_3CH_2C^*OH$ species, and this would lead to rates inhibited by H_2, inconsistent with observed rate data (Fig. 2b).

The irreversible nature of the steps forming $CH_3CH_2C^*OH$ (Step 24) and cleaving C–O bonds (Steps 16, 19, 21, 22, 25, and 26), taken together with the quasi-equilibrated nature of alkanol-alkanal interconversions (Section 3.1), makes it possible to isolate the first irreversible step for each of the C–O activation routes in Scheme 5 (Rxns. 16, 19, 22, 21, 24, and 25). The C-O bond activation step is the first irreversible step in all cases, except in the $CH_3CH_2C^*OH$-mediated route, for which $CH_3CH_2C^*OH$ formation is the first irreversible step (Step 24).

C–O hydrogenolysis rates are independent of H_2 pressure (Fig. 2b). Direct C–O activation of propanol (Rxn. 16 in Scheme 5) and H*-assisted C–O activation of $CH_3CH_2CH^*OH$ species (Rxn. 21) both lead to rate equations independent of H_2 pressure and thus consistent with measured rate data. Other C–O activation routes (via Rxns. 19, 22, 24, or 25) are mediated by kinetically-relevant transition states with fewer H-atoms than alkanol reactants, making rates sensitive to H_2 inconsistent with measured rates (Fig. 2b). Nevertheless, we consider them here for completeness. C–O cleavage in $CH_3CH_2CH_2O^*$ (Step 19) or $CH_3CH_2CHOH^*$ (Step 22) intermediates and the formation of $CH_3CH_2COH^*$ species (Step 24) all occur after one H-removal step from propanol, leading to rates inversely proportional to H_2 pressure because the kinetically-relevant transition state has one fewer H-atom than the relevant precursors (gas-phase propanol):

$$\frac{r}{[L]} = \frac{\beta(BuOH)}{(H_2)^{0.5}\left(1+K_{CO}(CO)\right)^2} \tag{S19}$$

These three routes (C–O cleavage via Step 19, 22, and 24) all follow Equation S19 and thus their rate ratios are independent on H_2 pressure. $\Delta H^{\neq}$ values for these reactions indicate that $CH_3CH_2COH^*$ formation rates ($\Delta H^{\neq}_{24}$

= 123 kJ mol^{-1}) are 2.0 x10^{7} times faster (at 523 K) than rates of $CH_3CH_2CHOH^*$ activation ($\Delta H^{\ddagger}_{22}$ = 196 kJ mol^{-1}) and $CH_3CH_2CH_2O^*$ activation ($\Delta H^{\ddagger}_{19}$ = 214 kJ mol^{-1}). The ratio of rates of C–H activation of $CH_3CH_2CHOH^*$ to form $CH_3CH_2COH^*$ (Rxn 24) and H*-assisted C–O activation of $CH_3CH_2CHOH^*$ (Rxn 21):

$$\frac{r_{24}}{r_{21}} = \frac{A_{24}[*]}{A_{21}[H^*]} e^{\left(\frac{\Delta H_{act,21} - \Delta H_{act,24}}{RT}\right)} \tag{S20}$$

depends on H* concentration (which varies with H_2 pressure) and because H* coverage is not kinetically-relevant (i.e. H* is not a MASI), it is difficult to estimate for this system. Furthermore, because $\Delta H_{\mathrm{act},21}$ and $\Delta H_{\mathrm{act},24}$ are similar (38 and 60 kJ mol^{-1}, respectively), the exponential term in Equation S20 (6.4 x10^{-3}) is close enough to 1 to prevent any meaningful conclusions on the rate ratio because [*]/[H*] is greater than 1 at these conditions. For completeness, we use DFT-estimated frequencies here to estimate entropies (and free energies) of transition states and reactive intermediates, however, low-wavenumber frequencies obtained from DFT are not very accurate and contribute most significantly to entropies (and thus free energies), making conclusions which significantly rely on these values spurious compared to conclusions made based on estimations of ΔH_{act} and $\Delta H^{\ddagger}$. Rewriting Equation S20 in terms of effective free energies:

$$\frac{r_{24}}{r_{21}} = \frac{1}{(H_2)^{0.5}} e^{\left(\frac{\Delta G_{act,21} - \Delta G_{act,24}}{RT}\right)} \tag{S21}$$

gives a ratio dependent upon H_2 pressure (in units of bar) and a difference in ΔG_{act} values. The difference in ΔG_{act} can be written in terms of free energies of individual species:

$$\Delta G_{\mathrm{act},21} - \Delta G_{\mathrm{act},24} = G[\mathrm{TS}_{21}^{**}] - G[\mathrm{TS}_{24}^{**}] - 0.5\, G[\mathrm{H_2(g)}] \tag{S22}$$

which is independent of the free energy of H* and is -8 kJ mol^{-1} (at 1 bar and 523 K) indicating that the rate ratio (Eq. S21) is less than 0.01 at H_2 pressures greater than 1.6 bar (0.16 MPa) H_2. These DFT-derived free energies suggest that H*-assisted C–O activation of hydroxypropyl prevails over C–H activation to form $CH_3CH_2COH^*$ (which rapidly undergoes C–O activation) at H_2 pressures relevant to this study (greater than 1 MPa), consistent with the measured independence in turnover rates with H_2 pressure.

Section S8. Effects of Particle Size on Rate Constants

The effects of Ir cluster size (Fig. 7) on decarbonylation (Eq. 2) and C–O (Eq. 6) hydrogenolysis turnover rates reflect the effects of surface coordination on the lumped rate constants (α and β for decarbonylation and C–O hydrogenolysis, respectively) and the CO adsorption constants (K_{CO}). The decarbonylation lumped rate constant (α) includes the rate constant for the kinetically-relevant step ($k_{CH,3}$) and the equilibrium constants for the preceding steps (Scheme 2):

$$\alpha = K_{BuOH}K_{OH,1}K_{CH,1}K_{CH,2}K_{H_2}^{-1.5}k_{CH,3} \tag{S23}$$

which becomes, using the formalism of transition state theory:

$$\alpha = \frac{k_BT}{h}e^{\left(\frac{-\Delta G_{\text{eff,C–C}}}{RT}\right)} \tag{S24}$$

With:

$$\Delta G_{\text{eff,C–C}} = \Delta G_{\text{BuOH}} + \Delta G_{\text{OH,1}} + \Delta G_{\text{CH,1}} + \Delta G_{\text{CH,2}} - 1.5\Delta G_{\text{H}_2} + \Delta G^{\ddagger}_{\text{CH,3}} \tag{S25}$$

where these free energy differences are based on the elementary steps in Scheme 2. This equation becomes:

$$\Delta G_{\text{eff,C-C}} = G^{\ddagger}_{\text{CH,3}} - 2G_* + 1.5G_{\text{H}_2} - G_{\text{BuOH}} \tag{S26}$$

in terms of the free energies of the kinetically-relevant transition state ($G^{\neq}_{CH,3}$), bare sites (G_*) and the gaseous H_2 (G_{H2}) and 1-butanol (G_{BuOH}) reactants. Similarly, the effective rate constant for C-O hydrogenolysis (β) is:

$$\beta = K_{\text{BuOH}}K_{\text{CH}}k_{\text{C–O}} \tag{S27}$$

$$\beta = \frac{k_BT}{h}e^{\left(\frac{-\Delta G_{\text{eff,C–O}}}{RT}\right)} \tag{S28}$$

$$\Delta G_{eff,C-O} = \Delta G_{BuOH} + \Delta G_{CH} + \Delta G^{\ddagger}_{C-O} \tag{S29}$$

$$\Delta G_{eff,C-O} = G^{\ddagger}_{C-O} - 2G_* - G_{BuOH} \tag{S30}$$

where free energies in Eq. S29 are based on elementary steps in Scheme 4 and the free energies of the kinetically-relevant transition state for C–O hydrogenolysis ($G^{\neq}_{C–O}$) appears in Eq. S30. Bond-order conservation considerations would suggest that low-coordination atoms bind all adsorbed species (including transition states) more strongly;[57] thus, C–O and C–C hydrogenolysis rates would be higher on smaller clusters, but only at conditions of low CO* coverages, for which α and β solely determine turnover rates, but not for the turnover rates but not for the turnover rates reported in Figure 10a measured at conditions (1 kPa CO) that lead to significant CO* coverages.

At high CO* coverages, Equation 7 becomes

$$\frac{r}{[L]} = \frac{\alpha'(BuOH)}{(H_2)^{1.5}(CO)^2} \tag{S31}$$

$$\alpha' = \frac{\alpha}{K_{CO}^2} \tag{S32}$$

and α’ and K_{CO} are given by:

$$\alpha' = \frac{k_B T}{h} e^{\left(\frac{-\Delta G'_{\text{eff,C-C}}}{RT}\right)} \tag{S33}$$

$$K_{CO} = e^{\left(\frac{-\Delta G_{ads,CO}}{RT}\right)} \tag{S34}$$

where $\Delta G'_{\text{eff,C-C}}$ is:

$$\Delta G'_{eff,C-C} = \Delta G_{eff,C-C} - 2\Delta G_{ads,CO} \tag{S35}$$

and $\Delta G_{ads,CO}$ is:

$$\Delta G_{ads,CO} = G_{CO^*} - G_{CO} - G_* \tag{S36}$$

thus leading to:

$$\Delta G'_{eff,C-C} = G^{\ddagger}_{CH,3} - 2G_{CO^*} + 1.5G_{H_2} + 2G_{CO} - G_{BuOH} \tag{S37}$$

Similar equations for C–O hydrogenolysis are:

$$\frac{r}{[L]} = \frac{\beta'(BuOH)}{(CO)^2} \tag{S38}$$

$$\beta' = \frac{\beta}{K_{CO}^2} \tag{S39}$$

$$\beta' = \frac{k_B T}{h} e^{\left(\frac{-\Delta G'_{\text{eff,C-O}}}{RT}\right)} \tag{S40}$$

$$\Delta G'_{eff,C-\mathrm{O}} = \Delta G_{eff,C-\mathrm{O}} - 2\Delta G_{ads,CO} \tag{S41}$$

$$\Delta G'_{eff,C-O} = G^{\ddagger}_{C-O} - 2G_{CO^*} + 2G_{CO} - G_{BuOH} \tag{S42}$$

Surface atoms of low coordination bind both transition state but also CO* more strongly. At high CO* coverages, it is the relative effects of coordination on ΔG_{eff} and $\Delta G_{\text{ads,CO}}$ (and thus $G^{\neq}_{\text{CH,3}}$ or $G^{\neq}_{\text{C–O}}$ as well as $G_{\text{CO*}}$) that determine their preference for atoms with a given coordination. Higher decarbonylation turnover rates on smaller particles indicate that low coordination atoms favor the binding of its kinetically-relevant transition state over the two CO* species that must be removed to bind it, while the opposite is the case for C–O hydrogenolysis reactions on Ir clusters. These considerations are illustrated by the sketch of a reaction coordinate in Figure S16. The free energy associated with CO* adsorption is always more negative on corners and edges ($\Delta G^{c/e}_{ads,CO}$) than on terraces ($\Delta G^{ter}_{ads,CO}$):

$$-\Delta G^{c/e}_{ads,CO} > -\Delta G^{ter}_{ads,CO} \tag{S43}$$

Similarly, the ΔG_{eff} values for both reactions are less positive on corner and edge sites than on terrace sites.

$$\Delta G^{c/e}_{eff,C-C} < \Delta G^{ter}_{eff,C-C} \tag{S44}$$

$$\Delta G^{c/e}_{eff,C-O} < \Delta G^{ter}_{eff,C-O} \tag{S45}$$

Thus, decarbonylation occurs preferentially on smaller particles because its transition state is better stabilized on low-coordination atoms than CO* (Fig. S16A),

$$\left(\Delta G^{c/e}_{eff,C-C} - \Delta G^{ter}_{eff,C-C}\right) < \left(2\Delta G^{c/e}_{ads,CO} - 2\Delta G^{ter}_{ads,CO}\right) \tag{S46}$$

leading to lower $\Delta G'_{\text{eff}}$ values (Eq. S37) than on terraces. The opposite trends for C–O hydrogenolysis reactions indicate that low-coordination atoms stabilize its transition state less effectively than the two CO* molecules that must be removed to bind it (Fig. S16B),

$$\left(\Delta G^{c/e}_{eff,C-O} - \Delta G^{ter}_{eff,C-O}\right) > \left(2\Delta G^{c/e}_{ads,CO} - 2\Delta G^{ter}_{ads,CO}\right) \tag{S47}$$

The kinetically-relevant transition state for decarbonylation has two C–M bonds (of 204 and 232 pm) as well as one H–M bond (163 pm) (Fig. 8a), whereas that for C–O hydrogenolysis contains just one C–M bond (213 pm) and one H–M bond (183 pm) (Fig. 8b). These number of attachments to the surface for each kinetically-relevant transition state and their distances indicate that the decarbonylation transition state is more strongly-bound to the surface than that for C–O hydrogenolysis, which proceeds via activation of the C–O bond by vicinal H* instead of metal-atom insertion into a C–H bond, as in decarbonylation. The greater role of the metal surface in the decarbonylation transition state implies that it will be more greatly stabilized by decreasing metal-atom coordination than that for C–O hydrogenolysis:

$$\left(\Delta G^{c/e}_{eff,C-C} - \Delta G^{ter}_{eff,C-C}\right) < \left(\Delta G^{c/e}_{eff,C-O} - \Delta G^{ter}_{eff,C-O}\right) \tag{S48}$$

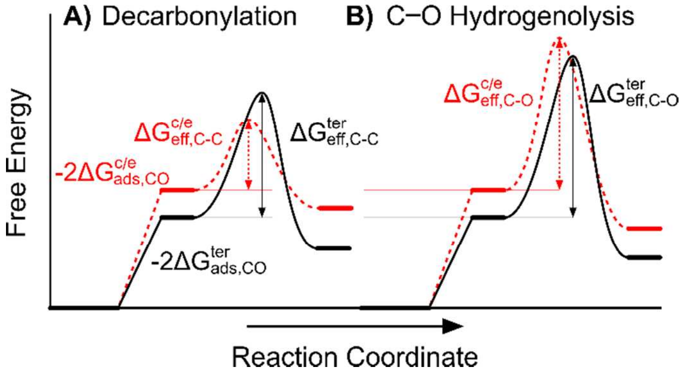

Figure S16. Qualitative reaction coordinate diagram for **A)** decarbonylation and **B)** C–O hydrogenolysis on lower-coordinated corner/edge atoms and higher-coordinated terrace atoms. Labeled free-energy differences include: adsorption energies for CO* on corner/edge sites ($\Delta G^{c/e}{}_{ads,CO}$) and on terrace sites ($\Delta G^{ter}{}_{ads,CO}$), the effective free energy barriers for forming decarbonylation transition states on corner/edge sites ($\Delta G^{c/e}{}_{eff,C-C}$) and on terrace sites ($\Delta G^{ter}{}_{eff,C-C}$), and those for C–O hydrogenolysis ($\Delta G^{c/e}{}_{eff,C-O}$ and $\Delta G^{c/e}{}_{eff,C-O}$).